Fluid Dynamics of Flow Through Microscale Lattice Structures Formed from Self-Propagating Photopolymer Waveguides

Kathryn D. Fink, Joanna A. Kolodziejska, Alan J. Jacobsen, and Christopher S. Roper
HRL Laboratories, LLC, Malibu CA, 90265

DOI 10.1002/aic.12490
Published online December 29, 2010 in Wiley Online Library (wileyonlinelibrary.com).

The fluid dynamics of flow through microscale lattice structures is characterized for different unit cell sizes, flow angles, and flow rates. The structures consist of an octahedral-type periodic unit cell, which is formed from an interconnected pattern of self-propagating photopolymer waveguides. The periodic unit cell of each sample has a node-to-node spacing between 800 and 2400 μm and a truss member diameter between 148 and 277 μm. Water is directed through the microscale lattice structures, and the resulting pressure drop is investigated for two different flow angles and superficial flow rates between 0.5 and 4.8 L/min. Finite element analysis is used to determine pressure drop in the laminar flow regime. The results are used to develop a correlation describing friction factor as a function of flow direction, geometric characteristics, and Reynolds number. This work enables control of the fluid dynamics in microarchitected multifunctional truss materials through design and superficial flow angle. © 2010 American Institute of Chemical Engineers *AIChE J,* 57: 2636–2646, 2011
Keywords: fluid dynamics, porous material, open cellular material, Ergun equation, multifunctional material

Introduction

Fluidic devices and systems with features in the microscale are of increasing interest in a number of areas, including mass transfer, micromixers and microreactors, and other small-scale chemical processing techniques.[1] Both heat,[2,3] and mass transfer[4] per unit area scale inversely with characteristic channel width. Furthermore, the surface area to volume ratio of microfluidic devices and systems is significantly enhanced as compared to the macroscale, increasing efficiency per unit volume. The ability to use small fluid volumes minimizes transient conduction times, decreasing the energy required to reach steady state and allowing for faster diffusion times in chemical processing.[5] Microfluidic flow control is simplified by the dominance of viscous over inertial forces, maintaining flow within the laminar regime. Likewise, capillary forces become significant at the microscale[6] and can be used to drive flow in heat pipes[7] and other devices.[8]

These numerous beneficial properties of microscale fluidic devices and systems have led to the integration of miniaturized flow control devices onto a single device for lab-on-a-chip applications. Common lab-on-a-chip components include valves,[9] reactors,[10] pumps,[11] and micromixers.[12] Patterning additional features in microscale channels further enhances chaotic advection at low Reynolds numbers;[13] controlled flow through such features can also achieve turbulence whereas maintaining uniform mixing at a minimal flow rate.[14] The advantages of microscale flow conducive to lab-on-a-chip applications also result in favorable conditions for fast, controlled chemical reactions. This has resulted in the development of microreactors composed of thin catalysts

Correspondence concerning this article should be addressed to C. S. Roper at csroper@hrl.com.

with microscale features, with the resulting high surface areas per length or volume of such structures offering an ideal environment for catalysis or mass transfer.[15,16] The mass transfer coefficients of packed-bed reactors at this size scale have been experimentally shown to be multiple orders of magnitude greater than their macroscale counterparts.[17] However, three-dimensional microfabrication techniques such as LIGA,[18] UV lithography using SU-8 photoresist,[19] microstereolithography,[20] and multistep rapid prototyping[21] present limitations in the maximum thickness, surface area,[22] production costs and creation of three-dimensional complexity, thereby restricting the range of possible Reynolds numbers and reagent quantities.

Microfluidic benefits also apply for macroscale fluid volumes moving through microscale channels or openings. Porous random packings such as Raschig rings,[23] Berl saddles and Pall rings have historically dominated the field of packed-bed reactors,[24] but the complexity of these structures complicates prediction of important parameters such as pressure drop.[25,26] Ordered packings such as Montz and Koch Sulzer packings have lower pressure loss compared to random packings[27]; in addition, their predictable geometry makes them more conducive to characterization based on interfacial area.[28] One area of possible future growth in this field is the application of predictable microscale features to the porous packing model.[29]

Open-cell metallic foams are an alternative to random packings that cover a range of porosities and feature sizes. With an average pore diameter in the range of millimeters, open-cell foams have characteristics favorable for fluidic applications including heat transfer,[30] catalysis, and mass transfer.[31] Although a variety of manufacturing processes exist for these stochastic materials, these processes result in some variation of the unit cell characteristics throughout a given sample.[32,33] Imperfections such as remaining cell wall boundaries and excess solid material at cell strut intersections affect the dynamics of fluid flow through these foams,[34] resulting in the same characterization issues as random packings.

Periodic and quasi-periodic structures such as metal textiles and lattice materials with features in the microscale have also been investigated; their ordered structure minimizes fluid pressure drop, resulting in through-flow efficiency several orders of magnitude better than open-cell foams.[35] Lattice truss structures have the highest efficiency while minimizing overall weight and offer the ability to support mechanical loads. However, manufacturing methods including investment casting, wire lay-up, folding perforated metal sheets, or by assembling individual truss lengths onto predrilled face sheets are complicated and often costly.[36,37] Furthermore, all of these methods have been demonstrated with a minimum cell size of several millimeters, well above the ideal range for microfluidics.

A novel process has recently been developed for the fabrication of highly ordered and scalable polymer lattice structures with unit cell feature sizes in the range of tens to hundreds of micrometers.[38–40] The microscale lattice structures are formed from an interconnected three-dimensional pattern of self-propagating photopolymer waveguides. Unlike other lithographic techniques, this process can be used to make thick (>10 mm) three-dimensional open-cellular structures from a single two-dimensional exposure surface. The unit cell geometry and resulting porosity of this microscale lattice structure are easily manipulated by altering the mask pattern and incident angle of UV light. This allows creation of a wide array of structures with unit cell features in the desirable microfluidics length scale[41] without retooling equipment or altering fabrication procedures. Fabrication duration for the polymer structure is on the order of tens of seconds, a significant reduction compared to other traditional techniques. The mechanical load-bearing properties of this structure make it ideal for multifunctional applications.[39,40] Like other lattice-frame materials, the periodic nature of the microscale lattice structure is favorable for heat and mass transfer and pressure loss characterization, with the additional advantage of feature sizes spanning the entire microfluidic range.

In this work, we investigate the fluid dynamics of flow through this microscale lattice structure using both experimental methods and finite element analysis. An equation is developed correlating friction factor and Reynolds number by analyzing the fluid pressure drop along the length of a section of microscale lattice over a range of flow rates, superficial flow angles and unit cell sizes in the intermediate and turbulent regime, and finite element analysis results in the laminar regime. The results describe the flow behavior across a wide range of microscale lattice architectures, fluids, and flow conditions.

Methods

Microscale lattice fabrication

Open-cellular polymer microscale lattice samples are fabricated from an interconnected pattern of self-propagating photopolymer waveguides.[38] For this study, all samples are made with an octahedral-type unit cell having D_{4h} group symmetry as depicted in Figure 1a. For this unit cell architecture, the process involves exposing a mask with a square pattern of circular apertures placed adjacent to a reservoir of the photosensitive monomer precursor. The mask is exposed simultaneously to four collimated beams generated from a mercury arc lamp. Each collimated beam has a 40° incident angle off the mask surface but is rotated 90° about the mask normal; due to the refractive index of the mask substrate, the resulting waveguides have an angle (θ) of $\sim$60° to the mask surface. The resulting structures are postcured for 24 hours at 100 °C to improve stiffness and cross-linking of the polymer waveguides, resulting in a glassy, nondeforming structure under flow conditions. Using the same photopolymer chemistry as Jacobsen et al.,[38] the resulting contact angle is 39°, measured by an A-100 Rame-Hart goniometer. Further details regarding the polymer microscale lattice fabrication process can be found elsewhere.[39,41]

The size of the unit cell and the relative density of the microscale lattice are controlled by varying the aperture size (D) and the spacing between adjacent nodes (L) (Figure 1a). Relative density is inversely proportional to the square of the aspect ratio L/D. Additionally, relative density is observed to scale inversely with aperture size for a constant L/D. This is attributed to an increase in polymer residue near the nodes of the cured waveguides.[39]

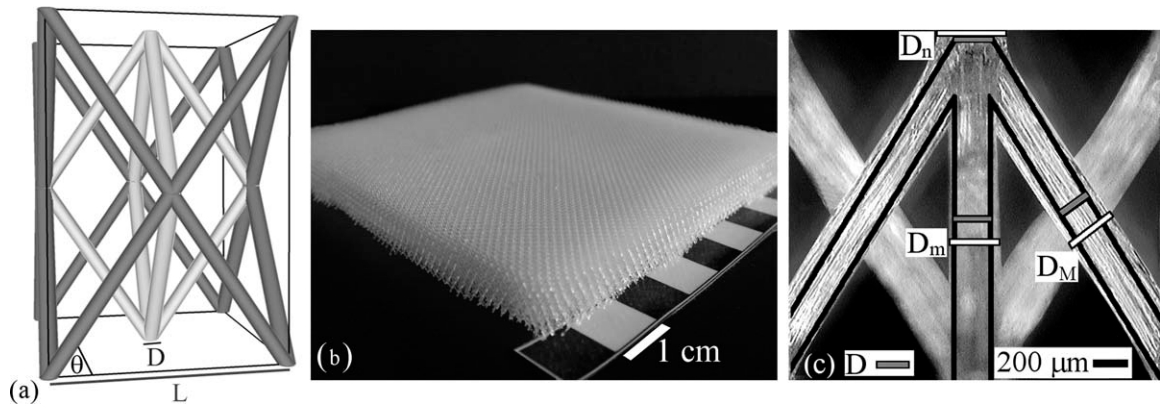

Figure 1. (a) Schematic of the octahedral-type repeating unit cell; (b) photo of fabrication-size microscale lattice sample; (c) comparison of actual half unit cell structure (micrograph image) and predicted structure (outline).

Microscale lattice samples are fabricated using masks with aperture diameters of 100, 158, and 200 μm and L/D ratios of 8, 10, and 12. The number of repeating unit cells through the thickness of each sample depends on the L/D ratio; however, all samples tested in this work are a minimum of 3 unit cells thick to minimize the influence of the effect of the test chamber walls. Figure 1b depicts the overall dimensions of an exemplar sample.

Optical micrographs of each sample in the 45° orientation are analyzed to obtain precise measurements of truss and node diameters as well as truss angle. To account for variation among unit cells within a sample, truss dimensions are measured for an equal number of unit cells at the top, middle and bottom of the sample. Fabricated unit cell length L remains equal to mask node spacing; however, fabricated truss diameters are greater than the mask aperture size D. In the orientation in Figure 1c, it is observed that the angled truss members have a diameter (D_M) which is on average 5% larger than the truss member projected vertically (D_m) to the plane of orientation, indicating slightly elliptical cross sections. The intersection of four elliptical members results in roughly circular nodes with a diameter D_n. The projection of the truss diameter in the 0° orientation ($D_{0°}$) is calculated from D_M, D_m, and θ. Figure 1c compares the expected unit cell dimensions as calculated from the mask dimensions (outline) with the actual resulting unit cell for a characteristic example.

The relative density (ρ/ρ_s) is calculated based on the known solid density of the polymer,[38] $\rho_s = 1340$ kg/m^3 and the measured mass and outer volume of each respective sample (sample absolute density ρ). Open volume fraction (ε_v) is then calculated from $1-(\rho/\rho_s)$. Eq. 1 specifies the open area ratio (ε_A) for a 0° superficial flow angle with truss angle of θ'; ε_A for a 45° superficial flow angle is given by Eq. 2. The derivation of Eqs. 1 and 2 can be found in the Appendix.

$$\varepsilon_{A(0^o)} = \left(1 - \frac{\sqrt{2}}{(L/D_{0^o})\sin\theta'}\right)^2 \tag{1}$$

$$\varepsilon_{A(45^\circ)} = \frac{4\left(\frac{L}{2} - \frac{D_m}{2} - \frac{D_M}{2\sin\theta}\right)^2}{L^2} \tag{2}$$

Table 1 provides mask dimensions and resulting unit cell dimensions for each sample. Micrographs of each sample in the 45° orientation are shown in Figure 2.

Experimental procedure

To determine friction factor for each unit cell geometry, a 2.6 cm by 10.2 cm microscale lattice sample 1 cm thick is placed in the fluidic test chamber of identical interior dimensions. Deionized water is run through the fluidic test chamber by a Trident Engineering M1443 pump, with flow rate monitored by a Cynergy3 ultrasonic flowmeter (Figure 3a). Differential pressure is measured with an Omega PX2300 differential pressure transducer between the inlet and each of

Table 1. Microscale Lattice Sample Characteristics

Mask Dimensions			Actual Truss Dimensions							Open Area Ratio	
L/D	$D(\mu m)$	$L(\mu m)$	L/D_n	$D_n(\mu m)$	$D_M(\mu m)$	$D_m(\mu m)$	θ	ρ/ρ_s	ε_v	$\varepsilon_A(0°)$	$\varepsilon_A(45°)$
8	100	800	3.21	250 ± 32	179 ± 20	165 ± 12	58.1°	0.254	0.746	0.443	0.281
8	158	1264	3.86	327 ± 45	253 ± 22	230 ± 7	57.9°	0.201	0.799	0.493	0.339
8	200	1600	4.28	374 ± 40	225 ± 56	261 ± 15	56.9°	0.171	0.829	0.587	0.447
10	100	1000	4.17	240 ± 17	183 ± 16	160 ± 19	55.6°	0.158	0.842	0.528	0.382
10	158	1580	4.84	326 ± 57	252 ± 18	235 ± 46	57.3°	0.146	0.854	0.576	0.437
10	200	2000	5.19	385 ± 58	277 ± 17	280 ± 19	56.0°	0.128	0.872	0.612	0.481
12	100	1200	5.17	232 ± 31	157 ± 19	148 ± 11	53.2°	0.089	0.911	0.633	0.509
12	158	1896	6.65	285 ± 54	211 ± 23	202 ± 14	57.1°	0.074	0.926	0.689	0.579
12	200	2400	6.33	379 ± 62	265 ± 45	244 ± 25	55.9°	0.069	0.931	0.692	0.585

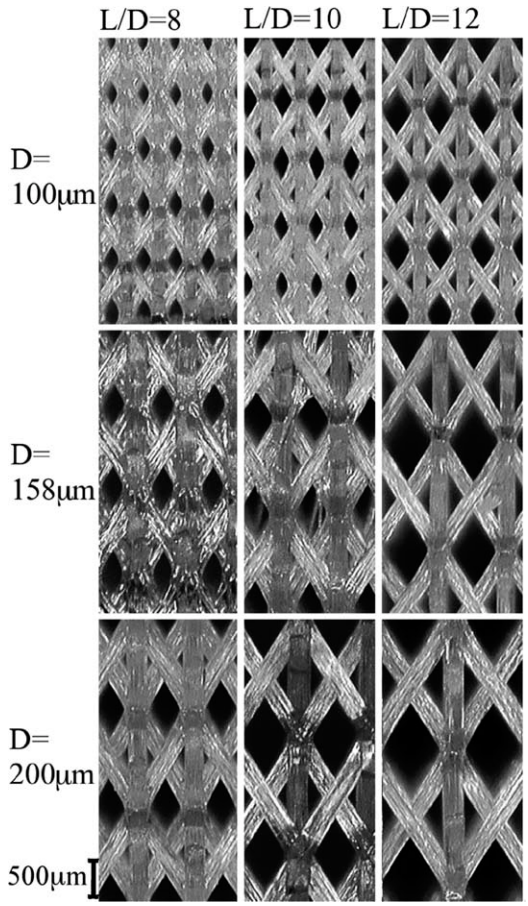

Figure 2. Optical micrographs of microscale lattice samples with varying mask dimensions L and D, and constant collimated beam angle of 40° to mask surface rotated 90° about mask normal.

five pressure ports beginning 1.3 cm past the inlet and spaced 1.9 cm apart along the centerline of the test chamber lid. (Figure 3b). Each pressure port is 2 mm in diameter, on the equivalent size scale as the unit cell length. This diameter ensures that the average pressure along a unit cell is measured, negating any variations in measured pressure due to localized cell features. Once the sample is in place and before data collection, the system is run at the maximum pump flow rate through a continuous path comprising the sample chamber, each successive pressure port and an outlet channel until all air bubbles have been removed from the tubing and sample chamber.

The collected data is used to determine the pressure loss between the first port and each subsequent downstream port. A linear fit is calculated to yield the pressure drop per unit length ($\Delta P/l$) for each combination of microscale lattice sample and flow rate. Superficial velocity (U) for a fluid of density ρ_f and viscosity μ is calculated from flow rate and chamber cross-sectional area normal to the superficial flow direction. Average velocity is then obtained by dividing superficial velocity by the open volume fraction (ε_v) of the material.

The length scale chosen for Reynolds number (Re_n) is the measured node width.

$$Re_n = \frac{\rho_f U D_n}{\mu \varepsilon_v} \tag{3}$$

Darcy friction factor (f) is then determined for each sample and flow condition.

$$f = \left(\frac{\Delta P}{l}\right) \frac{2D_n}{\rho_f (U/\varepsilon_v)^2} \tag{4}$$

For each unit cell geometry, the procedure is completed for two orientations of the microscale lattice sample within the fluidic test chamber, equivalent to two superficial flow directions offset by 45° in the horizontal plane. The difference in these offset flow paths for the different flow directions can be seen in Figure 4a. A superficial flow angle of 0° creates complete unit cell alignment, resulting in unobstructed diamond-shaped channels in the flow direction spanning the entire length of the sample (Figure 4b). A 45° offset to the flow angle introduces an additional vertical strut normal to the flow direction, while additionally imposing a half unit cell offset between successive cells rows (Figure 4c).

Results and Discussion

Experimental results

The resulting correlations of pressure drop per unit length for samples oriented at 0° to the superficial flow direction

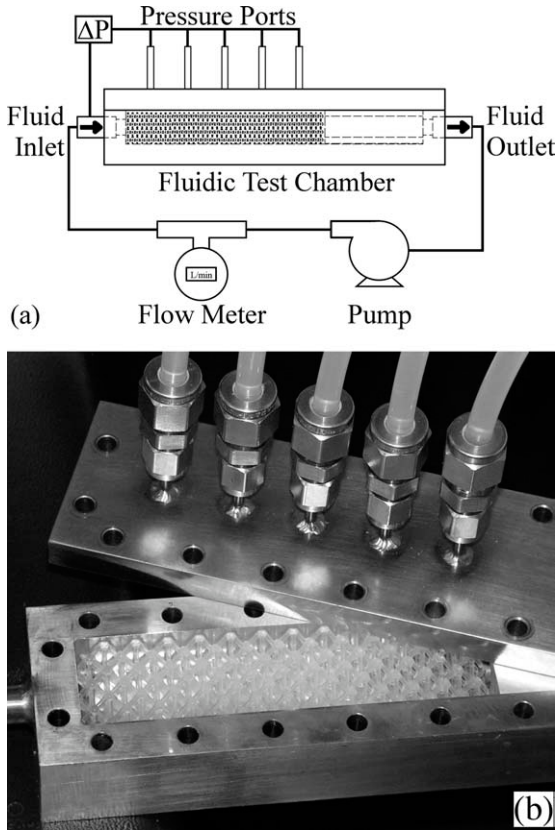

Figure 3. (a) Schematic of fluid flow test setup. (b) Image of fluidic test chamber with sample.

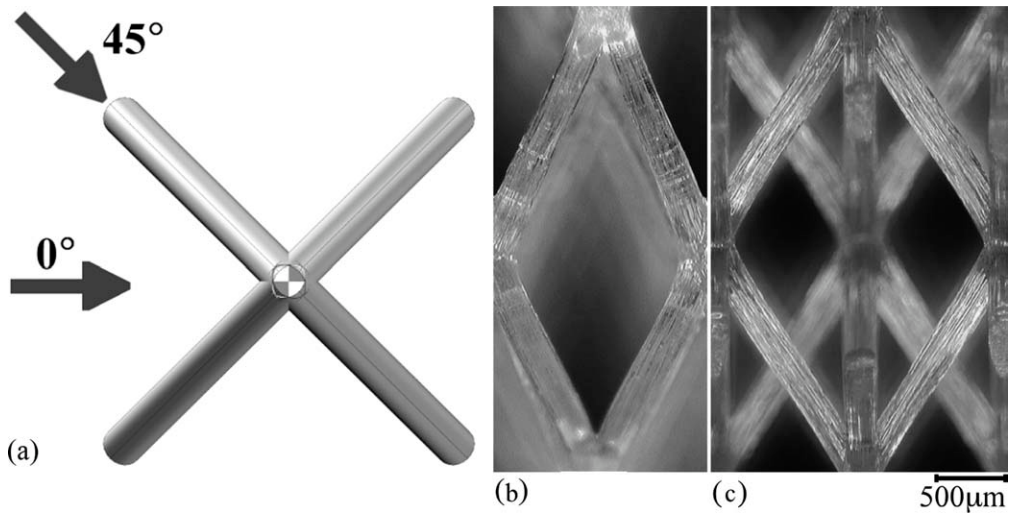

Figure 4. Images of a microtruss unit cell depicting the flow angles: (a) schematic top-view indicating both superficial flow directions, (b) optical micrograph side view with unit cell oriented at 0° to superficial flow direction, and (c) optical micrograph side view with unit cell oriented 45° to superficial flow direction.

exhibit variations between microscale lattice samples of differing geometry, as illustrated in Figure 5. Pressure drop per unit length increases monotonically with superficial velocity in all cases, as expected. For samples with the same aperture diameter, pressure drop per unit length is greatest for the least porous samples ($L/D = 8$) and smallest for the most porous samples ($L/D = 12$). This trend is consistent across all sets of geometries. In addition, for samples with the same mask L/D ratio, the least porous samples consistently have the largest pressure drop, while the most porous samples have the smallest.

When the results are translated to the dimensionless parameters of friction factor and Reynolds number, the dependencies of pressure loss or friction factor on sample architecture become more apparent. The order of the data sets from high to low friction factor at a given Reynolds number shown in Figure 6a reflects a similar trend as observed in Figure 5. The data in this flow regime is scaling approximately with the inverse square root of Reynolds number. This indicates intermediate flow between the laminar, or Darcy, regime where the friction factor scales proportionally with the inverse of Reynolds number and the turbulent regime where the friction factor is independent of Reynolds number.

For each microscale lattice sample, friction factor for the 45° superficial flow direction (Figure 6b) was significantly greater than in the 0° flow direction (Figure 6a). While the observed trends in Figures 5 and 6a were influenced by porosity, the porosity of a single sample tested at different flow orientations remains constant. It is therefore clear that the orientation of the unit cell to the flow affects friction factor by altering the open area ratio (ε_A) normal to the flow direction as previously illustrated in Figure 4. Pressure loss in the transition and turbulent regimes can therefore be tailored based solely on orientation for a single geometry or relative density.

Finite element analysis results

A computer-aided design model of a single unit cell is constructed for use in finite element analysis of flow in the laminar regime, outside of the measurement range of the experimental setup. The Incompressible Navier-Stokes application mode in COMSOL Multiphysics 3.5a is used to simulate low Reynolds number flow through a unit cell. No-slip boundary conditions are applied to all truss walls. Symmetric boundary conditions are applied to the top, bottom, and side unit cell boundaries and periodic boundary conditions are applied to the unit cell inlet and outlet to simulate flow through a large structure composed of repeating unit cells in three-dimensions. A mesh refinement study is performed to assure solutions were independent of mesh size; meshes with greater than forty thousand elements are selected as a compromise between accuracy and computational expense (Figure 7).

The mask dimensions used in creating experimental samples are applied to the unit cell model, representing an

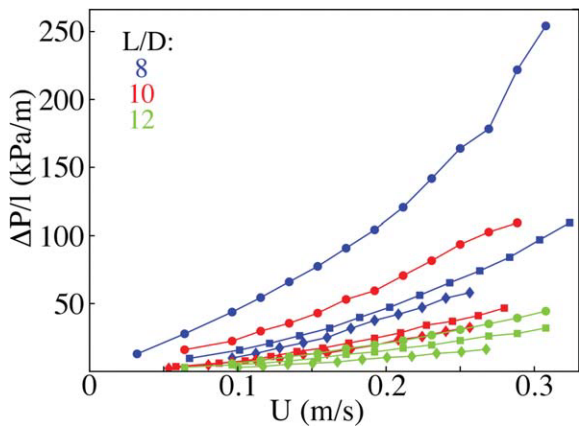

Figure 5. Pressure drop per unit length (ΔP/l) vs. superficial flow velocity (U) for flow oriented at 0° to microscale lattice for (○) $D = 100$ μm, (□) $D = 158$ μm and (◇) $D = 200$ μm.

[Color figure can be viewed in the online issue, which is available at wileyonlinelibrary.com.]

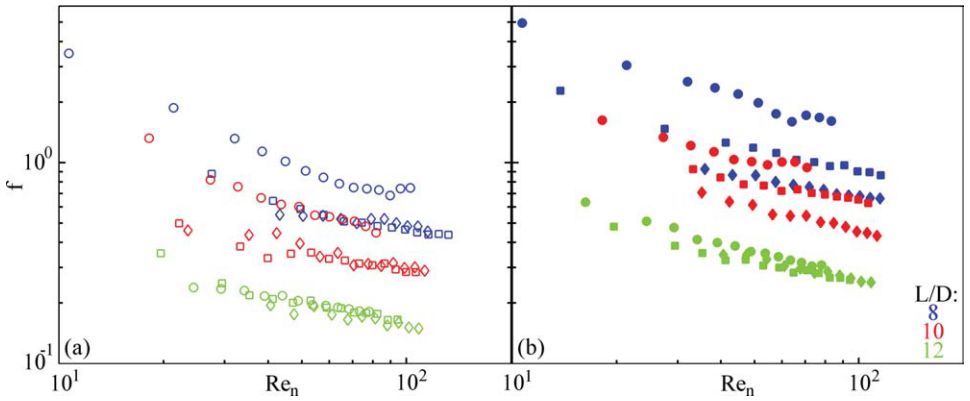

Figure 6. Friction factor versus Reynolds number for flow oriented at (a) 0° and (b) 45° to microscale lattice for (○) D = 100 μm, (□) D = 158 μm and (◇) D = 200 μm.

[Color figure can be viewed in the online issue, which is available at wileyonlinelibrary.com.]

idealized geometry consisting of struts with circular cross sections. Pressure at one point in the unit cell is specified and, at each selected Reynolds number, the simulation solves for pressure drop across a unit cell to achieve the specified average volumetric flow rate. As with the experimental data, friction factor and Reynolds number are then calculated for each case. The results shown in Figure 8 present a definite correlation between friction factor and L/D ratio, with only a minimal dependence on truss diameter and unit cell length. Mass is conserved to better than 0.14% for each simulation, with an average mass change of 0.06%.

To quantify the observed correlation between friction factor and L/D ratio, simulations are executed at a single Reynolds number with unit cell L/D ratios ranging from 6 to 14, as shown in Figure 9. Nonlinear least squares data fitting is performed based on an equation of $f = C_1(L/D)^{-C_2}$. The resulting value for C_2 is equal to 8/3, accurate to six decimal places.

Development of correlation equation

Numerous previous studies characterizing fluid flow through microchannels[42] and macroscale lattice frame materials[43–45] are examined. However, the unit cell size, periodic arrangement, porosity and flow angle dependence of the presented microscale lattice structure are unique compared to previous microscale studies. Characterization based on friction factor equations for diamond-shaped channels or angled and staggered banks of tubes fails to yield a satisfactory correlation equation. The unit cells studied by Kim and Lu[46] are geometrically similar to the microscale unit cell; however, their work occurred at the macroscale with 2 mm truss diameters. Furthermore, the half-unit cell thickness of the samples examined in the works by Lu et al. and the presence of a sharp transition between laminar and turbulent flow at a Reynolds number of 2100 suggests their measured pressure loss was dominated by channel flow rather than effects from the lattice frame material. In contrast, the range of three to six unit cell thick samples tested in this study are likely sufficient to minimize wall effects, as demonstrated by the smooth transition between flow regimes.

The Ergun equation[47] most closely resembles the friction factor behavior of the microscale lattice materials, with a smooth transition from laminar flow ($f = C_L/\mathrm{Re}$) through the intermediate regime ($f \approx C_t/\sqrt{\mathrm{Re}}$) into turbulent flow ($f = C_T$). The traditional form of the equation describes flow through a packed bed, and has been applied to numerous packed-bed reactor materials. However, the higher porosity of the microscale lattice structure as compared to traditional

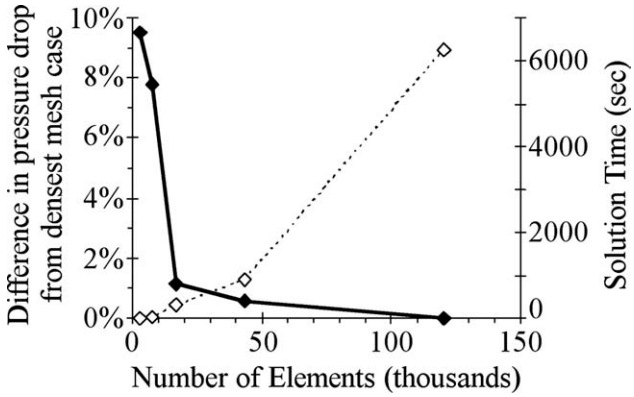

Figure 7. Data from mesh refinement study.

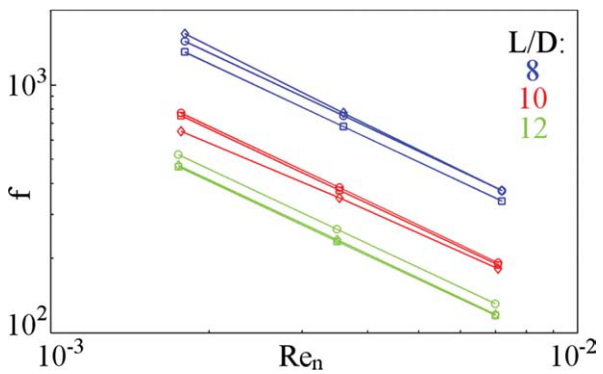

Figure 8. Friction factor versus Reynolds number from finite element analysis for flow oriented at 0° to microscale lattice for (○) D = 100 μm, (□) D = 158 μm and (◇) D = 200 μm.

[Color figure can be viewed in the online issue, which is available at wileyonlinelibrary.com.]

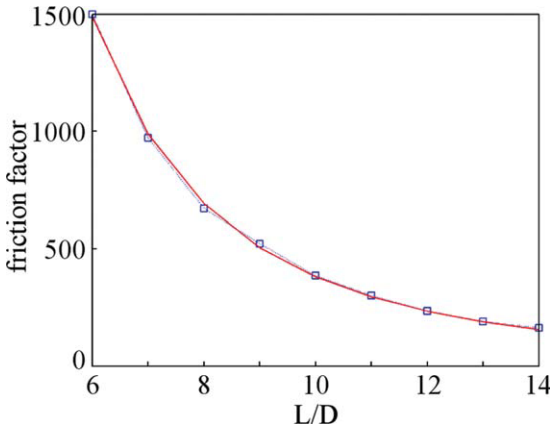

Figure 9. Finite element friction factor values (□) at Reynolds number 4 × 10^{-3} for varying simulated *L/D* unit cell ratios.

The fitted line is $C^*(L/D)^{-8/3}$, where C is a constant related to Reynolds number. [Color figure can be viewed in the online issue, which is available at wileyonlinelibrary.com.]

packed beds results in unsatisfactory fitting using the Ergun equation constants ($A = 150$, $B = 1.75$). The functional form of the Ergun equation (Eq. 5) is used as the basis for a fitting equation, with fitting for the constants A and B.

$$f = \frac{A}{\mathrm{Re}} + B \tag{5}$$

A factor of $(L/D_n)^{-8/3}$ is included in the laminar term as observed in the finite element analysis. The pressure loss coefficient geometric correlation term developed for flow through screens[48] and applied by Kim[49] to tetrahedral unit cells is included in the turbulent term to account for the observed difference in friction factor based on flow angle in the intermediate and turbulent regimes. A nonlinear least squares method is used to determine the constants A and B from Eq. 5 for friction factor in the 0° flow orientation (Eq. 6) and in the 45° direction (Eq. 7). In many flow conditions, the pressure loss is largely independent of the truss material used[43]; therefore, Eqs. 6 and 7 should apply not only to the polymer microscale lattice structures tested but also to ceramic or metal forms fabricated using the original polymer truss structures as templates.

$$f_{0^\circ} = \frac{729\left(\frac{L}{D_n}\right)^{-8/3}}{\mathrm{Re}_n} + 0.324\left(\frac{1-\varepsilon_{A(0^\circ)}}{\varepsilon_{A(0^\circ)}}\right)^2 \tag{6}$$

$$f_{45^\circ} = \frac{854\left(\frac{L}{D_n}\right)^{-8/3}}{\mathrm{Re}_n} + 0.242\left(\frac{1-\varepsilon_{A(45^\circ)}}{\varepsilon_{A(45^\circ)}}\right)^2 \tag{7}$$

When friction factor for each unit cell geometry is calculated from the fitting equation and plotted against the experimentally determined friction factor (Figure 10a), the comparison indicates a good fit for both the experimental and simulated samples. Furthermore, an analysis of the scaled residuals (Eq. 8) across the experimental regime yields no noticeable trends (Figure 10b). The $L/D = 10$, $D = 100$ μm data set is considered an outlier due to significant unit cell warping and residual polymer threads along the lower cell layers; it is the only sample with distinctly poor fitting in each of the residuals plots, and is not included in the fitting process to determine the equation constants.

$$\text{Scaled residual} = \frac{f_{\text{fitted}} - f_{\text{experimental}}}{f_{\text{experimental}}} \tag{8}$$

Further analysis of the residuals verifies the fitting equation does not result in any other deviation trends. Scaled residuals (Eq. 8) are plotted based on measured L/D_n ratios (Figure 11a) and node diameter D_n (Figure 11b). Once again, no trends are observed across all data sets, and the previously specified outlier set represents the only significant deviation.

To demonstrate the application of the fitting equation across the model and experimental data, finite element analysis for an additional unit cell is performed with geometry corresponding to the measured values of the $L/D = 12$, $D = 200$ μm sample of $L/D_n = 6.333$, $D = 250$ μm (Figure 12). Friction factor is calculated from the fitting equation based on the manufactured sample characteristics. The finite

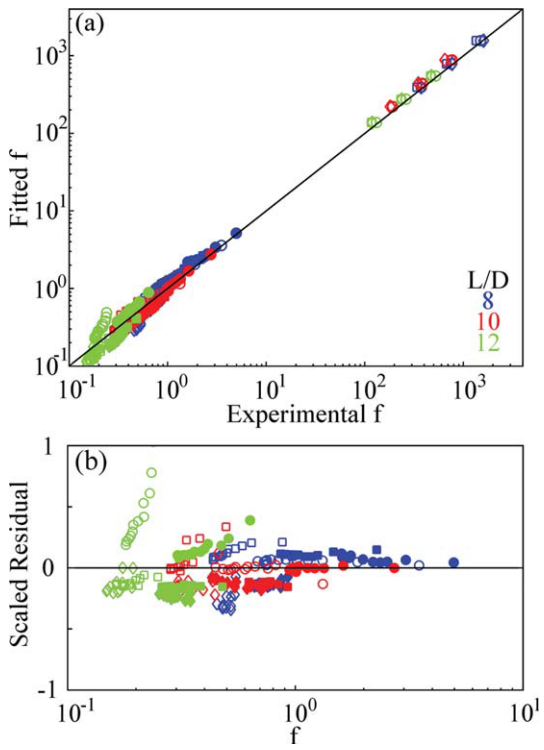

Figure 10. (a) Friction factor values obtained from the fitting equation versus friction factor values measured experimentally and with finite element analysis; (b) residuals from fitting equation normalized to experimental friction factor values for mask dimensions (○) *D* = 100 μm, (□) *D* = 158 μm and (◇) *D* = 200 μm.

Open symbols represent 0° flow angle and closed symbols represent 45° flow angle. [Color figure can be viewed in the online issue, which is available at wileyonlinelibrary.com.]

element data is on average 17% lower than the values predicted by the fitting equation.

Conclusion

The fluid dynamics of flow through microscale lattice structures with different unit cell sizes and relative densities is investigated. Characterization of fluid flow through the structures is performed across a variety of different flow conditions and by varying the superficial velocity and flow angle with respect to the unit cell orientation. The pressure drop data collected experimentally and through finite element analysis is used to develop a correlation between friction factor, Reynolds number, and geometric parameters based on the form of the Ergun equation. This demonstrates the ability to control fluid dynamics based on material microarchitecture and flow orientation.

Different physical properties of cellular materials generally display a similar dependence on the relative density of the material, and this dependence can lead to competing design constraints when considering multifunctional applications. For example, the mechanical properties of random open-cellular foams are positively correlated to relative density.[50] Likewise, there is a positive correlation between the relative density of foams and the associated fluidic pressure loss.[51] This means increasing a specific mechanical property, such as compression modulus, will require an increase in the relative density of the material; however, this will also result in an increase in the associated pressure loss for fluid flow through the material and increased pumping power demands. In contrast, this work shows increasing the relative density of the microscale lattice material can result in either an increase, decrease or no change in the pressure loss depending on the unit cell geometry and flow orientation, allowing independent control of fluidic and mechanical properties. In conjunction with the ease and flexibility of the fabrication process, this unique characteristic greatly enhances the multifunctional trade-space accessible by microscale lattice materials. Applications including *in situ* fabrication of mixing components on microfluidic devices or bulk generation of mechanically favorable, lightweight ordered packings are among the numerous potential microfluidic possibilities.

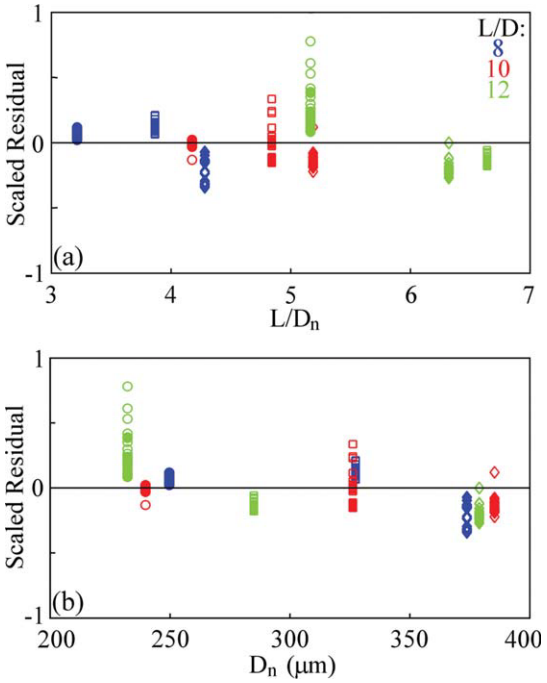

Figure 11. Plot of residuals from fitting equation normalized to experimental friction factor, grouped by (a) L/D_n ratio and (b) sample node diameter D_n for mask dimensions (○) D = 100 μm, (□) D = 158 μm and (◇) D = 200 μm.

Open symbols represent 0° flow angle and closed symbols represent 45° flow angle. [Color figure can be viewed in the online issue, which is available at wileyonlinelibrary.com.]

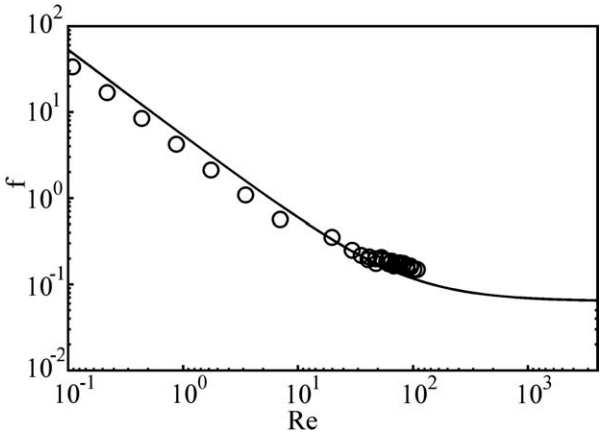

Figure 12. Plot of friction factor versus Reynolds number for a characteristic set of data from finite element analysis and experimental testing.

L/D_n ratio used is 6.333.

In summary, the correlation developed in this work provides a simple analytical equation to serve as the basis of design and numerical optimization of microfluidic applications of materials and systems incorporating the microscale lattice architecture, especially those encompassing heat or mass transfer. Combined with previous works,[39–41,52,53] the optimal design of architected, lightweight, multifunctional materials incorporating strength, stiffness, energy absorption, and/or fluidic functionalities is now enabled.

Notation

A = laminar constant in Ergun equation
B = turbulent constant in Ergun equation
C_1 = proportionality constant based on Reynolds number describing friction factor based on L/D
C_2 = exponential constant describing friction factor based on L/D
C_L = proportionality constant describing friction factor based on Reynolds number in laminar flow regime
C_t = proportionality constant describing friction factor based on Reynolds number in transition flow regime
C_T = proportionality constant describing friction factor based on Reynolds number in turbulent flow regime
D = mask aperture size (m)
D_M = major truss diameter normal to strut axis (m)
D_m = minor truss diameter normal to mask (m)
D_n = node diameter (m)

D_{0° = truss diameter projected in 0° orientation (m)
$\Delta P/l$ = pressure drop per unit length (Pa/m)
ε_V = open volume fraction (porosity)
ε_A = open area ratio
f = Darcy friction factor
L = mask cell length (m)
μ = Fluid viscosity (Pa s)
θ = truss angle relative to mask surface (°)
θ' = truss angle in 0° plane (°)
Re_n = Reynolds number based on node diameter
ρ = sample absolute density (kg/m^3)
ρ_f = fluid density (kg/m^3)
ρ_s = polymer bulk density (kg/m^3)
ρ/ρ_s = relative sample density
U = superficial fluid velocity (m/s)

Subscripts

A = area
Experimental = from experimental data
Fitted = calculated from fitting equation
f = referring to working fluid
M = referring to major truss diameter
m = referring to minor truss diameter
n = referring to node diameter
s = referring to bulk polymer
V = volume
0° = referring to 0° flow orientation
45° = referring to 45° flow orientation

Literature Cited

1. Whitesides GM. The origins and the future of microfluidics. *Nature*. 2006;442:368–373.
2. Evans AG, Hutchinson JW, Ashby MF. Multifunctionality of cellular metal systems. *Prog Mater Sci*. 1999;43:171–221.
3. Incropera FP, DeWitt DP, Bergman TL, Lavine AS. *Introduction to Heat Transfer*. Hoboken, NJ: Wiley, 2006.
4. Tonkovich ALY, Fitzgerald SP, Zilka JL, LaMont MJ, Wang Y, VanderWield DP, Wegeng RS. Microchannel chemical reactors for fuel processing application. II. Compact fuel vaporization. In: Proceedings of the IMRET: Industrial Prospects, Frankfurt, Germany; 2000;364–371.
5. Shopova SI, White IM, Sun Y, Zhu H, Fan X, Frye-Mason G, Thompson A, Ja S. On-column micro gas chromatography detection with capillary-based optical ring resonators. *Anal Chem*. 2008; 80:2232–2238
6. Vogel MJ, Ehrhard P, Steen PH. The electroosmotic droplet switch: countering capillarity with electrokinetics. *Proc Natl Acad Sci USA*. 2005;102:11974–11979.
7. Reay DA, Kew PA. *Heat Pipes: Theory, Design and Applications*, *5th ed*. Butterworth-Heinemann: Oxford, 2006.
8. Borno RT, Steinmeyer JD, Maharbiz MM. Charge-pumping in a synthetic leaf for harvesting energy from evaporation-driven flows. *Appl Phys Lett*. 2009;95:013705.
9. Oh KW, Ahn CH. A review of microvalves. *J Micromech Microeng*. 2006;16:R13.
10. Doku GN, Verboom W, Reinhoudt DN, van den Berg A. On-microchip multiphase chemistry—a review of microreactor design principles and reagent contacting modes. *Tetrahedron*. 2005;61: 2733–2742.
11. Laser DJ, Santiago JG. A review of micropumps. *J Micromech Microeng*. 2004;14:R35–R64.
12. Mansur EA, Ye M, Wang Y, Dai Y. A state-of-the-art review of mixing in microfluidic mixers. *Chinese J Chem Eng*. 2008;16: 503–516.
13. Nguyen N-T, Wu Z. Micromixers—a review. *J Micromech Microeng*. 2005;15:R1–R16.
14. Schönfeld F, Hessel V, Hofmann C. An optimized split-and-recombine micro-mixer with uniform 'chaotic' mixing. *Lab Chip*. 2004; 4:65–69.
15. Ameel TA, Warrington RO, Wegeng RS, Drost MK. Miniaturization technologies applied to energy systems. *Energy Convers Manag*. 1997;38:969–982.
16. Chambers RD, Spink RCH. Microreactors for elemental fluorine. *Chem Commun*. 1999;10:883–884.
17. Losey MW, Schmidt MA, Jensen KF. Microfabricated multiphase packed-bed reactors: characterization of mass transfer and reactions. *Ind Eng Chem Res*. 2001;40:2555–2562.
18. Menz W, Bacher W, Harmening M, Michel A. The LIGA technique—a novel concept for microstructures and the combination with Si-technology by injection molding. In: Proceedings of the MEMS' 1991, IEEE, Nara, Japan, 1991:69–73.
19. Lin C-H, Lee G-B, Chang B-W, Chang G-L. A new fabrication process for ultra-thick microfluidic microstructures utilizing SU-8 photoresist. *J Micromech Microeng*. 2002;12:590–597.
20. Zhang X, Jian XN, Sun C. Micro-stereolithography of polymeric and ceramic microstructures *Sens Actuators*. 1999;77:149–156.
21. Anderson JR, Chiu DT, Jackman RJ, Cherniavskaya O, McDonald JC, Wu H, Whitesides SH, Whitesides GM. Fabrication of topologically complex three-dimensional microfluidic systems in PDMS by rapid prototyping. *Anal Chem*. 2000;72:3158–3164.
22. Harris C, Despa M, Kelly K. Fabrication of a cross flow micro heat exchanger. *J Microelectromechs*. 2000;9:502–508.
23. Shulman HL, DeGouff JJ. Mass transfer coefficients and interfacial areas for 1-inch raschig rings. *Ind Eng Chem*. 1952;44:1915–1922.
24. Perry RH, Green DW. *Perry's Chemical Engineers' Handbook*, *7th ed*. New York: McGraw Hill, 1997.
25. Bravo JL, Fair JR. Generalized correlation for mass transfer in packed distillation columns. *Ind Eng Chem Process Des Dev*. 1982; 21:162–170
26. Wagner I, Stichlmair J, Fair JR. Mass transfer in beds of modern, high-efficiency random packings. *Ind Eng Chem Res*. 1997;36:227–237.
27. Chung T-W, Ghosh TK. Comparison between random and structured packings for dehumidification of air by lithium chloride solutions in a packed column and their heat and mass transfer correlations. *Ind Eng Chem Res*. 1996;35:192–198.
28. Fair JR, Seibert AF, Behrens M, Saraber PP, Olujic Z. Structured packing performance—experimental evaluation of two predictive models. *Ind Eng Chem Res*. 2000;39:1788–1796.
29. Jensen, KF. Microreaction engineering—is small better? *Chem Eng Sci*. 2001;56:293–303.
30. Lu TJ, Stone HA, Ashby MF. Heat transfer in open-cell metal foams. *Acta Mater*. 1998;46:3619–3635.
31. Giani L, Groppi G, Tronconi E. Mass-transfer characterization of metallic foams as supports for structured catalysts. *Ind Eng Chem Res*. 2005;44:4993–5002.
32. Wadley HNG. Cellular materials manufacturing. *Adv Eng Mater*. 2002;4:726–733.
33. Banhart J. Manufacture, characterization and application of cellular metals and metal foams. *Prog Mater Sci*. 2001;46:559–632.
34. Bhattacharya A, Calmidi VV, Mahajan RL. Thermophysical properties of high porosity metal foams. *Int J Heat Mass Transf*. 2002;45:1017–1031.
35. Lu TJ, Valdevit L, Evans AG. Active cooling by metallic sandwich structures with periodic cores. *Prog Mater Sci*. 2005;50:789–815.
36. Wadley HNG. Multifunctional periodic cellular materials. *Philos Trans R Soc A*. 2006;364:31–68.
37. Joo J-H, Kang B-S, Kang K-J. Experimental studies on friction factor and heat transfer characteristics through wire-woven bulk Kagome structure. *Exp Heat Transfer* 2009;22:99–116.
38. Jacobsen AJ, Barvosa-Carter W, Nutt S. Micro-scale lattice structures formed from self-propagating photopolymer waveguides. *Adv Mater*. 2007;19:3892–3896.
39. Jacobsen AJ, Barvosa-Carter W, Nutt S. Compression behavior of micro-scale lattice structures formed from self-propagating polymer waveguides. *Acta Mater*. 2007;55:6724–6733.
40. Jacobsen AJ, Barvosa-Carter W, Nutt S. Shear behavior of polymer micro-scale lattice structures formed from self-propagating polymer waveguides. *Acta Mater*. 2008;56:1209–1218.
41. Jacobsen AJ, Barvosa-Carter W, Nutt S. Micro-scale lattice structures with three-fold and six-fold symmetry formed from self-propagating polymer waveguides. *Acta Mater*. 2008;56:2540–2548.
42. Sobhan CB, Garimella SV. A comparative analysis of studies on heat transfer and fluid flow in microchannels. *Microscale Therm Eng*. 2001;5:293–311.
43. Kim T, Hodson HP, Lu TJ. Fluid-flow and endwall heat-transfer characteristics of an ultralight lattice-frame material. *Int J Heat Mass Transfer*. 2004;47:1129–1140.
44. Kim T, Hodson HP, Lu TJ. Contribution of vortex structures and flow separation to local and overall pressure and heat transfer

characteristics in an ultralightweight lattice material. *Int J Heat Mass Transfer*. 2005;45:4243–4264.
45. Joo J-H, Kang B-S, Kang K-J. Experimental studies on friction factor and heat transfer characteristics through wire-woven bulk Kagome structure. *Exp Heat Transfer*. 2009;22:99–116.
46. Kim T, Zhao CY, Lu TJ, Hodson HP. Convective heat dissipation with lattice-frame materials. *Mech Mater*. 2004;36:767–780.
47. Ergun S. Fluid flow through packed columns. *Chem Eng Prog*. 1952;48:89–94
48. Laws EM, Livesey JL. Flow through screens. *Ann Rev Fluid Mech*. 1978;10:246–266.
49. Tian J, Kim T, Lu TJ, Hodson HP, Queheillalt DT, Sypeck DJ, Wadley HNG. The effects of topology upon fluid-flow and heat-transfer within cellular copper structures. *Int J Heat Mass Transfer*. 2004;47:3171–3186.
50. Gibson LJ, Ashby MF. *Cellular Solids: Structure and Properties*, 2nd ed. New York: Cambridge University Press, 1988.
51. Liu JF, Wu WT, Chiu WC, Hsieh WH. Measurement and correlation of friction characteristic of flow through foam matrices. *Exp Therm Fluid Sci*. 2006;30:329–336.
52. Evans AG, He MY, Deshpande VS, Hutchinson JW, Jacobsen AJ, Carter WB. Concepts for enhanced energy absorption using hollow micro-lattices. *Int J Impact Eng*. 2010;37:947–959.
53. Roper CS. Multiobjective optimization for design of multifunctional sandwich panel heat pipes with micro-architected truss cores. *Int J Heat Fluid Fl*. http://dx.doi.org/10.1016/j.ijheatfluidflow.2010.07.002. 2010.

Appendix

ε_A for 0° superficial flow angle

When projected in the 0° orientation, the unit cells can be considered as repeating rhombuses. The geometry and associated dimensions for the unit cell in this orientation are shown in Figure A1. Due to the 45° offset of the unit cell from which θ is originally defined, the truss angle θ' is calculated from the measured truss angle θ as

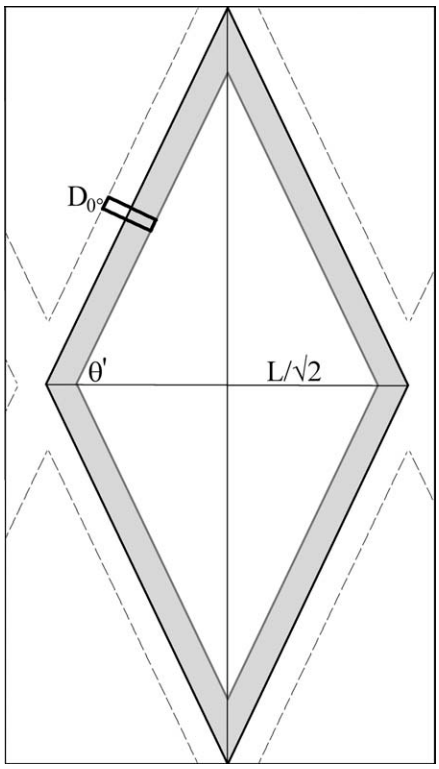

Figure A1. Projection of open area in 0° flow orientation.

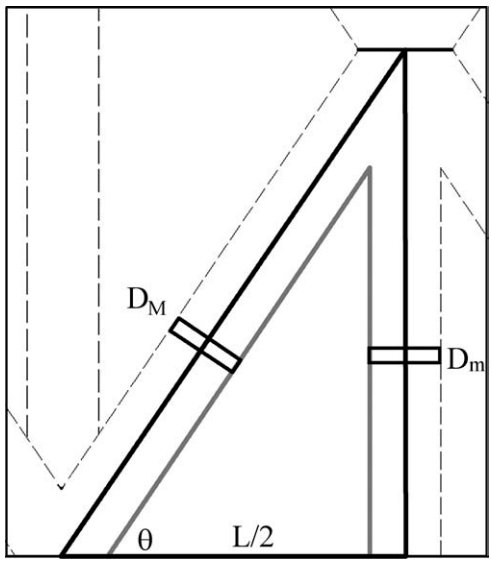

Figure A2. Projection of open area in 45° flow orientation.

$$\tan\theta' = \sqrt{2}\tan\theta \tag{A1}$$

Truss diameter D_{0° is then calculated as the projection of the diameter of an ellipse at an angle of 45° to its major/minor axes. The open area subset is equal to

$$A_{\text{open}} = \left(\frac{L}{\sqrt{2}} - \frac{D_{0^\circ}}{\sin\theta'}\right)\left(L\tan\theta - \frac{D_{0^\circ}}{\cos\theta'}\right) \tag{A2}$$

where

$$L\tan\theta = \frac{L}{\sqrt{2}}\tan\theta' \tag{A3}$$

The overall area is

$$A_{\text{total}} = \left(\frac{L}{\sqrt{2}}\right)\left(\frac{L}{\sqrt{2}}\tan\theta'\right) \tag{A4}$$

Thus the open area fraction in the 0° orientation is

$$\varepsilon_{A(0^\circ)} = \frac{2\left(L/\sqrt{2} - D_{0^\circ}/\sin\theta'\right)\left(L\tan\theta'/\sqrt{2} - D_{0^\circ}/\cos\theta'\right)}{L^2\tan\theta'} \tag{A5}$$

$$\varepsilon_{A(0^\circ)} = 2\left(\frac{1}{\sqrt{2}} - \frac{D_{0^\circ}/L}{\sin\theta'}\right)\left(\frac{1}{\sqrt{2}} - \frac{D_{0^\circ}/L}{\cos\theta'}\frac{\cos\theta'}{\sin\theta'}\right) \tag{A6}$$

$$\varepsilon_{A(0^\circ)} = \left(1 - \frac{\sqrt{2}}{(L/D_{0^\circ})\sin\theta'}\right)^2 \tag{A7}$$

ε_A for 45° superficial flow angle

The unit cell projected normal to the 45° flow direction is composed of eight identical triangular subsets from which the open area can be calculated, as shown for a partial unit cell in Figure A2.

The base of the triangle representing open area is

$$\frac{L}{2} - \frac{D_m}{2} - \frac{D_M}{2\sin\theta} \tag{A8}$$

with a corresponding height of

$$\left(\frac{L}{2} - \frac{D_m}{2} - \frac{D_M}{2\sin\theta}\right)\tan\theta \tag{A9}$$

The total area is

$$\frac{1}{2}\left(\frac{L}{2}\right)\left(\frac{L}{2}\tan\theta\right) \tag{A10}$$

The open area ratio is therefore

$$\varepsilon_{A(45^\circ)} = \frac{\frac{1}{2}\left(\frac{L}{2} - \frac{D_m}{2} - \frac{D_M}{2\sin\theta}\right)^2\tan\theta}{\frac{1}{8}L^2\tan\theta} \tag{A11}$$

which simplifies to

$$\varepsilon_{A(45^\circ)} = \frac{4\left(\frac{L}{2} - \frac{D_m}{2} - \frac{D_M}{2\sin\theta}\right)^2}{L^2} \tag{A12}$$

Manuscript received July 7, 2010, and revision received Sept. 24, 2010.